Laser wakefield: Experimental study of nonlinear radial electron oscillations

J. R. Marquès, F. Dorchies, F. Amiranoff, P. Audebert, J. C. Gauthier, and J. P. Geindre
Laboratoire pour l'Utilisation des Lasers Intenses, Ecole Polytechnique-CNRS, 91128 Palaiseau, France

A. Antonetti
Laboratoire d'Optique Appliquée, Ecole Nationale Supérieure des Techniques Avancées, 91128 Palaiseau, France

T. M. Antonsen, Jr.
IPRDEEP, University of Maryland, College Park, Maryland 20742

P. Chessa and P. Mora
Centre de Physique Théorique, Ecole Polytechnique-CNRS, 91128 Palaiseau, France

(Received 19 August 1997; accepted 14 November 1997)

The plasma electron density oscillation produced in the wake of a narrow (beam waist$\ll$plasma wavelength) ultrashort laser pulse is measured by frequency-domain interferometry with a temporal resolution much better than the electron plasma period, and a spatial resolution across the laser focal spot. The absolute density perturbation is observed to be maximum when the pulse duration equals half the plasma period. The relative density perturbation varies from a few percent at high density to 100% at low density. For nonlinear oscillations we measure the increase of the electron plasma frequency predicted for radial oscillations [J. M. Dawson, Phys. Rev. **113**, 383 (1959)]. The damping of the oscillations is observed. It is very rapid (a few periods) when the oscillation is nonlinear. Comparison with the code WAKE [P. Mora and T. M. Antonsen, Jr., Phys. Rev. E **53**, R2068 (1996)] indicates that the gas ionization creates a steep radial density gradient near the edge of the focus and that the electrons oscillating near this density gradient are responsible for the damping. © *1998 American Institute of Physics.* [S1070-664X(98)00103-7]

I. INTRODUCTION

The accelerating electric field in conventional accelerators is limited to around 100 MV/m by the breakdown on the structures. Fully ionized plasmas can sustain electron plasma waves (EPW) with relativistic phase velocities and electrostatic fields that can exceed 100 GV/m,[1] making them very attractive as compact high-energy particle accelerators or sources.[2] The ponderomotive force of an intense laser pulse can excite such waves via the laser beat-wave (LBW),[3] the laser wakefield (LWF),[3] or the self-resonant laser wakefield processes (SRLWF).[4] Several experiments have observed the acceleration of injected electrons by the LBW[5–8] and the LWF,[9] or of background electrons by the SRLWF.[9,10] Electric fields of the order of 1 GV/m for the LBW or the LWF, and of 100 GV/m for the SRLWF have been produced. An overview of these methods and experiments can be found in Ref. 11. These experiments have demonstrated the feasibility of each concept. However, only a few of them have measured the EPW[6,8] and identified the mechanisms that limit its amplitude and lifetime.

Particle accelerators require a longitudinal electric field. The resonant excitation of the LWF is mainly longitudinal if $\sigma \gg c\tau_0$,[11–13] where σ is the laser focal spot radius and τ_0 is the pulse duration. The maximum longitudinal field is given by: $E_z(\mathrm{GV/m}) \approx 8.2\times 10^{-19} I(\mathrm{W/cm^2})\lambda^2(\mu\mathrm{m})/\tau_0(\mathrm{ps})$. Reaching $E_z \geq 1$ GV/m with a Ti:sapphire laser ($\lambda = 0.8\ \mu$m) of 1 J and 100 fs requires a focal spot radius $\sigma \approx 40\ \mu$m, leading to $\sigma \approx c\tau_0$. This means that with current lasers, transverse effects cannot be avoided, and a better knowledge of their influence is necessary.

Radial electron oscillations produced by the LWF process have recently been studied. Hamster *et al.*[14] have observed the quasiresonance of the LWF by measuring the terahertz electromagnetic emission of the EPW. However, the EPW period was not resolved and no spatial information was available. The electron density oscillations have been measured with a temporal resolution much better than the electron plasma frequency,[13,15] and spatial resolution in one dimension[13] in experiments using longitudinal frequency-domain interferometry of short laser pulses. With the same diagnostic, we have very recently[16] measured the temporal evolution of the EPW on a time scale much longer than the electron plasma period.

In this paper we present experiments in which we have measured radial electron plasma oscillations excited by laser wakefield using spatially resolved frequency-domain interferometry. The EPW amplitude, frequency, and damping are studied in detail around the LWF quasiresonance. The LWF theory and the difference between longitudinal and radial oscillations are presented rapidly in Sec. II and in more detail in Appendix A. The experimental setup and procedure are described in Sec. III, while an extensive discussion on the spatially resolved frequency-domain interferometry diagnostic is presented in Appendix B. Section IV is devoted to experimental results. In particular, we have observed the increase of the electron plasma frequency for nonlinear radial oscillations as predicted in Ref. 17. In this regime, we have also observed a very rapid damping (a few plasma periods) of the oscillation. We present simulation results obtained from the code WAKE indicating that gas ionization creates a steep radial density gradient near the edge of the focus. When the EPW reaches nonlinear amplitudes, the electron excursion is large enough to cross the radial density gradient. This nonharmonic motion leads to the damping of the oscillation. The codes WAKE and the code IMAGE that simulate the frequency-domain interferometry diagnostic are presented in Appendix C.

II. BASIC THEORY

A two-dimensional, nonrelativistic, analytical model of the LWF process has been developed by Gorbunov and Kirsanov.[12] This model is detailed in Appendix A. The electron motion is calculated assuming an electron density perturbation δn small compared to the equilibrium density n_e, fixed ions, and a cylindrical geometry. It is also assumed that the radial and temporal parts of the potential can be separated, which is valid for a Gaussian beam if the Rayleigh length $z_R = 2\pi\sigma^2/\lambda$ is much larger than $c\tau_0$ as it is actually the case in the experiment. The laser intensity in the vicinity of the focus can then be approximated by $I(r,z,t) = I_{\max}\exp(-r^2/\sigma^2)\exp[-(t-z/c)^2/\tau_0^2]$.

The electron density perturbation is excited by the ponderomotive force associated with the temporal and the radial profile of the short laser pulse. The electron density oscillation produced in the wake of the laser pulse is given by

$$\frac{\delta n}{n_e} = A\left[1+\left(\frac{2c}{\omega_{\mathrm{pe}}\sigma}\right)^2\left(1-\frac{r^2}{\sigma^2}\right)\right]\exp\left(-\frac{r^2}{\sigma^2}\right) \times\sin(\omega_{\mathrm{pe}}t-kz), \tag{1}$$

where

$$A \approx 21P(TW)\left(\frac{\lambda}{\sigma}\right)^2\left(\frac{\omega_{pe}\tau_0}{2}\right)\exp\left[-\left(\frac{\omega_{pe}\tau_0}{2}\right)^2\right]$$

is an amplitude factor characterizing the LWF quasiresonance (P is the laser pulse power at maximum and ω_{pe} is the electron plasma frequency, proportional to the square root of the electron density n_e).

The perturbation is the sum of two contributions: $\delta n = \delta n_z + \delta n_r$. The first one, δn_z, describes the longitudinal oscillation of the electrons. It is only induced by the temporal profile of the laser pulse. The second one, δn_r, corresponds to the transverse motion induced both by the temporal and radial profiles of the pulse. These perturbations are maximum when n_e satisfies $\omega_{pe}\tau_0 = \sqrt{6}$ for δn_z, and $\omega_{pe}\tau_0 = \sqrt{2}$ for δn_r and $\delta n_z/n_e$. The relative radial perturbation $\delta n_r/n_e$ has no resonance and increases when n_e decreases. The absolute and relative amplitudes of the radial and longitudinal perturbations versus electron density are shown in Fig. 1 for a pulse duration of 120 fs which corresponds to our experimental conditions.

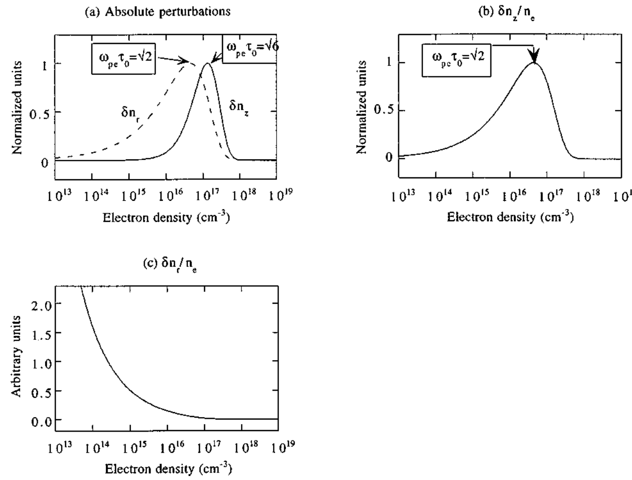

FIG. 1. (a) Absolute amplitudes of radial and longitudinal electron density perturbations versus the mean electron density: in our case the longitudinal contribution is absolutely negligible. (b) Relative amplitude of longitudinal perturbation. (c) Relative amplitude of radial perturbation (showing the absence of resonance).

The two contributions also have different transverse profiles. The radial dependence of the transverse and longitudinal part of the perturbation is shown in Fig. 2. Both of them present a radial extension of the order of the laser focal spot radius σ. The central part of the transverse perturbation comes from the initial radial expulsion of the electrons located near the high-intensity region $(r=0)$. These expelled electrons increase the electron density on both sides of the focus, thus creating the bumps around $r/\sigma = \sqrt{2}$.

The ratio of these contributions on the laser axis is $\delta n_r/\delta n_z(r=0) = (\lambda_p/\pi\sigma)^2$, where $\lambda_p = 2\pi c/\omega_{pe}$ is the plasma wavelength.

Therefore the electron motion can be treated as longitudinal when $\pi\sigma \gg \lambda_p$ and radial when $\pi\sigma \ll \lambda_p$. In this experiment, the density perturbation is observed with a diagnostic proportional to the product $L\,\delta n$, where the interaction length L is of the order of the laser Rayleigh length z_R. Equation (1) indicates that while the product $z_R\delta n$ is independent of σ for the longitudinal perturbation, it increases as $(\lambda_p/\sigma)^2$ for the transverse perturbation: $z_R\delta n_z \alpha P\lambda$ but $z_R\delta n_r \alpha P\lambda(\lambda_p/\sigma)^2$.

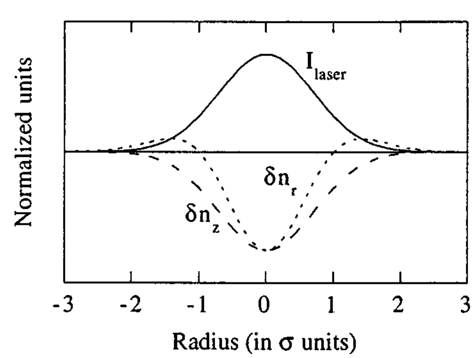

FIG. 2. Transverse profiles of the electron density perturbation: δn_z (dashed line), δn_r (dotted line). For the clarity of the graph, these amplitudes are multiplied by (-1). Solid line: laser intensity profile.

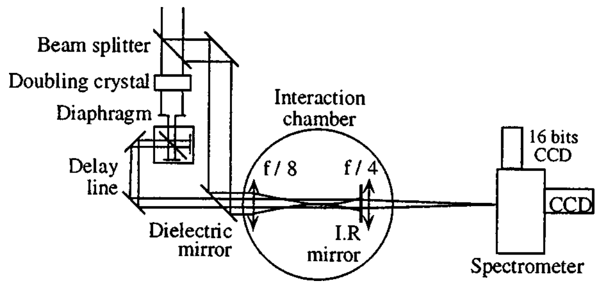

FIG. 3. Experimental setup.

The perturbation amplitude is maximum for a plasma wavelength λ_p that satisfies the quasiresonance condition $\omega_{pe}\tau_0 \approx 1$. For a given laser pulse (P and λ), the product $z_R \delta n_z$ is fixed, while the product $z_R \delta n_r$ can be increased by tightly focusing the laser beam (decreasing σ). The transverse oscillation then becomes much easier to measure than the longitudinal one. For these reasons, we have chosen to excite mainly the radial oscillation $[18 \leqslant (\lambda_p/\pi\sigma)^2 \leqslant 600$ in our experiment]. We can also reach the nonlinear regime more easily because δn_r is proportional to $(1/\sigma)^4$.

Let us note that if this radial oscillation (transverse field) may not be used for particle accelerators, it can be useful for photon acceleration:[18] the longitudinal density gradient required to shift the laser frequency is also present in a radial oscillation.

III. EXPERIMENTAL SETUP AND PROCEDURE

The principle of the experiment is the following: a pump beam is focused into a chamber backfilled with helium gas. The laser ionizes the gas near the focus and excites the electron perturbation. Two twin colinear probe pulses, separated in time and frequency doubled, are focused on the same axis. Because the group velocity of each probe pulse is almost equal to the phase velocity of the EPW, each pulse stays in phase with the density modulation during the propagation. If the electron densities seen by the pulses are different, their relative phase is modified during the propagation. We measure this relative phase shift by the spatially resolved frequency-domain interferometry technique[13] (see Appendix B): at the output of the plasma, the two probe pulses are time recombined: the temporal beating creates a system of fringes in the frequency domain. The position of the fringes depends on the relative phase between the two pulses. The easiest way to recombine the two pulses is to send them into a spectrometer: when the grating disperses the frequencies it also temporally stretches the pulses. The spatial information is obtained along the vertical slit of the spectrometer. The output spectrum is recorded on a charge-coupled device (CCD) camera. On each image, the horizontal axis gives the position of the fringes and so the perturbation amplitude, while the vertical axis gives a one-dimensional transverse resolution.

The experimental setup is shown in Fig. 3. The LOA 10 Hz Ti:Sapphire laser beam at a wavelength of 800 nm, with a maximum energy of 40 mJ and a duration of 120 fs [full width at half maximum (FWHM)], is split into two parts. The reflected part (80%) is used as the pump beam, and the transmitted part as the probe beam. The probe beam is frequency doubled and sent into a Michelson interferometer to generate two colinear pulses with an adjustable time delay. These two pulses pass through a circular aperture to improve the phase front homogeneity and increase their focal spot diameter to a size much larger than the pump one. The time delay between the pump and the probe pulses is adjusted with a delay-line. The probe beam is injected colinearly with the pump by transmission through a dichroic mirror that reflects the pump. The pump and probe pulses are focused by a f/8 MgF_2 lens in a low-pressure helium gas (around 1 mbar). The gas pressure is measured with a precision of ± 1 μbar by a capacitance manometer.

The pump focal spot is almost Gaussian with a radius (at $1/e$ of the maximum intensity) $\sigma = 6 \pm 1$ μm, while the probe radius is 140 μm. The maximum pump intensity is 2×10^{17} W/cm^2, easily creating a fully ionized helium plasma in the focal area.[19] The focal plane is imaged on the spectrometer slit with a f/4 doublet, with a spatial resolution of about 2 μm and a magnification of 16. The pump beam is attenuated before the imaging lens by a dielectric mirror. The spectrometer slit is imaged on a CCD camera to control the alignment on the slit and the pump/probe spatial overlap.

We have designed our spectrometer to minimize the aberrations and the energy losses. This spectrometer uses one single spherical mirror (focal length of 1.5 m and aperture of f/18). The holographic grating is used near the Littrow angle. This configuration allows a reduction of the angle of incidence on the spherical mirror and thus minimizes the spherical aberration. It also minimizes the anamorphic magnification and maximizes the grating efficiency. With a 100 μm slit, the spectral resolution is 0.3 Å. At the output of the spectrometer, the twin probe pulses are stretched to 57 ps. The output spectrum is recorded on a 16 bit CCD camera.

The experimental procedure is the following: For each gas pressure, the time separation of the two probe pulses is adjusted to 1.5 T_{pe} ($T_{pe} = 2\pi/\omega_{pe}$ is the EPW period for a fully ionized helium gas). In this configuration, when one of the probe pulses coincides with a maximum of the density perturbation, the other pulse is located on a minimum. In that case, the phase difference between the two pulses corresponds to the peak-to-peak density perturbation. This optimizes the signal-to-noise ratio. It also avoids a contribution of the singly ionized region, the pulse separation being in that region almost equal to the electron period of the He^+ plasma.

Two modes of measurements are possible.[20] They are represented in Fig. 4. In the absolute mode, the first probe pulse propagates in the gas before the pump beam while the second one propagates in the plasma after the pump beam [Fig. 4(a)]. In this configuration, the phase shift between the pulses arises from the plasma formation. The amplitude and the spatial extent of this phase shift come from the integration along the laser axis in the singly and doubly ionized regions. This measurement also provides the absolute time separation Δt between the pump and the two probe pulses: we first adjust the pump–probe delay so that the probe pulses arrive before the pump pulse. As we decrease the delay, a

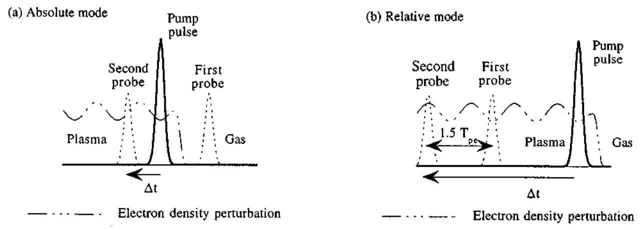

FIG. 4. Two modes of measurement: (a) the relative mode, (b) the absolute mode. The three pulses are collinearly propagating from the left to the right.

phase shift appears. It saturates when the second probe pulse is at the end of the ionization front. This corresponds to the pump pulse maximum ($\Delta t = 0$). In the relative mode, the two probe beams propagate after the pump beam, so that they both travel after the plasma formation [Fig. 4(b)]. Their relative phase is due to a plasma perturbation produced in the wake of the pump pulse. By recording the relative phase for various pump/probe time delays, one can measure the temporal evolution of the perturbation.

The spatial resolution of our frequency-domain interferometry enables us to probe both the perturbed and the unperturbed regions in a single shot. This provides a phase reference and avoids errors due to laser spectrum fluctuations. To eliminate errors due to the spectrometer slit imperfect quality (see Appendix B 4), we also substract the relative phase measured with a reference shot (shot without pump) to all other relative phase measurements.

IV. EXPERIMENTAL RESULTS

A. Spatial and temporal resolution

A typical result of the relative phase measurement is presented in Fig. 5. It has been obtained at a pressure of 0.5 mbar ($n_e = 2.5 \times 10^{16}$ cm^{-3} for fully ionized helium). Each vertical line is an average of 40 shots recorded at 10 Hz. The horizontal coordinate is the time delay Δt and the vertical coordinate is the radius from the laser axis. At $\Delta t < 0$ both the probe pulses propagate in the gas. When Δt increases, the second probe pulse begins to overlap with the pump pulse and is modified by the plasma formation. A relative phase shift appears (absolute mode, corresponding to part A

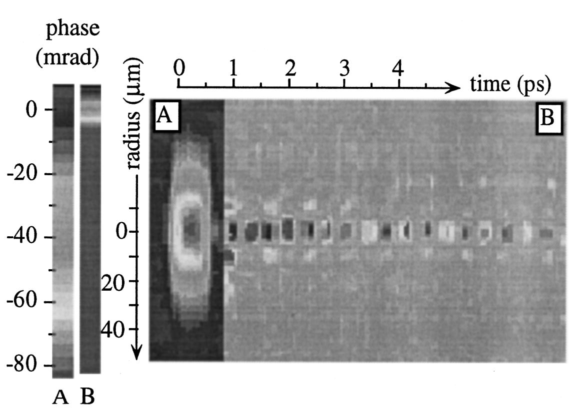

FIG. 5. Spatially and temporally resolved relative phase measurement with $n_e = 2.5 \times 10^{16}$ cm^{-3}. Part A and part B have different color scales.

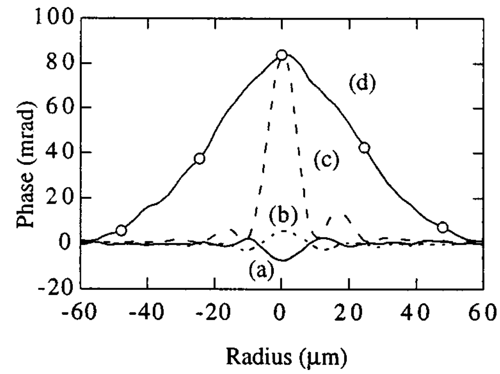

FIG. 6. Experimental radial profiles of the relative phase at a maximum (solid line), $0.5T_{pe}$ later (dotted line). Dashed line: measured intensity profile of the pump beam. Solid line with circles: maximum measured relative phase in the absolute mode.

of Fig. 5) and saturates when the second probe pulse arrives at the end of the ionization process. The phase shift decreases when the first probe pulse also begins to see the plasma. The continuous part of the relative phase shift then vanishes and only the oscillating part coming from the plasma perturbation (EPW) remains (relative mode presented with a different color scale in part B of Fig. 5).

Vertical line-outs of Fig. 5 are presented in Fig. 6. These radial profiles are the result of the integration of the relative phase shift along the propagation axis at each radius. The integration length is the minimum between the perturbation length and the Rayleigh length of the collecting optics. Curve (d) shows the transverse profile of the phase obtained in the absolute mode (part A of Fig. 5). This curve shows the radial plasma extent. Even if the helium gas is doubly ionized near the focus, the phase profile does not present a step-like shape. This is due to the integration along the laser axis (the radial location of the He^+/He^{2+} interface changes along the laser axis).

Curve (a) corresponds to a delay for which the phase amplitude is maximum in the relative mode. Because the amplitude of the laser wakefield is significant only in regions of high laser intensity ($r \leqslant \sigma$, $|z| \leqslant z_R$), the relative phase has a much smaller radial extent in part B than in part A. Curve (c) is the intensity profile of the pump focal spot. As expected from Eq. (1), the phase transverse profile of curve (a) presents two parts: a central part at $r < \sigma$ ($\approx 6\,\mu$m) and bumps on each side. Curve (b) is obtained half a plasma period later. As expected, it presents a reversed shape. We note that a flat profile (null phase) is measured when we delay the probe beams by a quarter of a plasma period after an extremum.

A horizontal line-out of Fig. 5 is presented in Fig. 7. It represents the relative phase on the laser axis as a function of time. The insert shows a vertical zoom of the phase oscillation in the relative mode, with a fit using an exponentially damped sinusoidal curve.

Typical measurements of the phase difference on the laser axis versus the pump/probe time delay are presented in Fig. 8 for various helium gas pressures. The different curves have been separated by 20 mrad. The relative accuracy in Δt

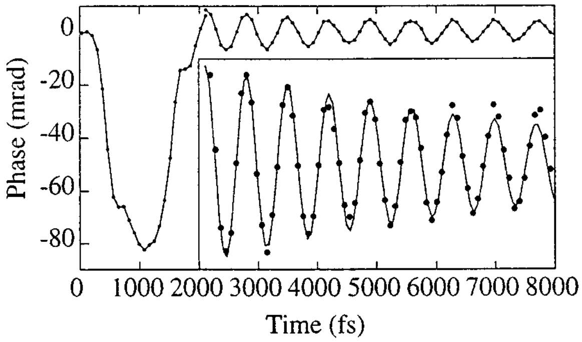

FIG. 7. Relative phase on the laser axis versus time (Δt) at $n_e = 2.5 \times 10^{16}\ \mathrm{cm}^{-3}$.

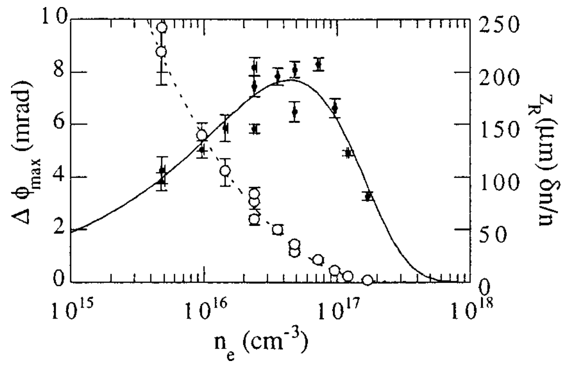

FIG. 9. Full circles: maximum relative phase on the laser axis versus the electron density. Solid line: numerical fit of the form $\delta n_{\max}(\omega_{pe}\tau_0) \times \exp[-2(\omega_{pe}\tau_0/2)^2]$. Open circles: relative density perturbation times the Rayleigh length calculated from the black circle's values. Dashed line: numerical fit of the form $B \exp[-C\omega_{pe}^2]/\omega_{pe}$.

is limited by the delay-line translation control digit and is better than 3 fs. The relative phase is oscillating with a well-defined period. As expected, this period decreases with the gas pressure. The phase difference is maximum around 1.5 mbar on the LWF quasiresonance. One can observe an important damping of the oscillation at lower pressures.

For each gas pressure, we apply to the curves of Fig. 8 a fit of the form: $\Delta\phi_{\max}*\exp[-\gamma(t-t_0)]*\sin[\omega_p(t-t_0)]$. The parameters of the fit are the maximum relative phase amplitude $\Delta\phi_{\max}$ the damping rate γ, and the frequency ω_p of the electron oscillation. We calculate the uncertainty of this numerical calculation and add it to the experimental error bars.

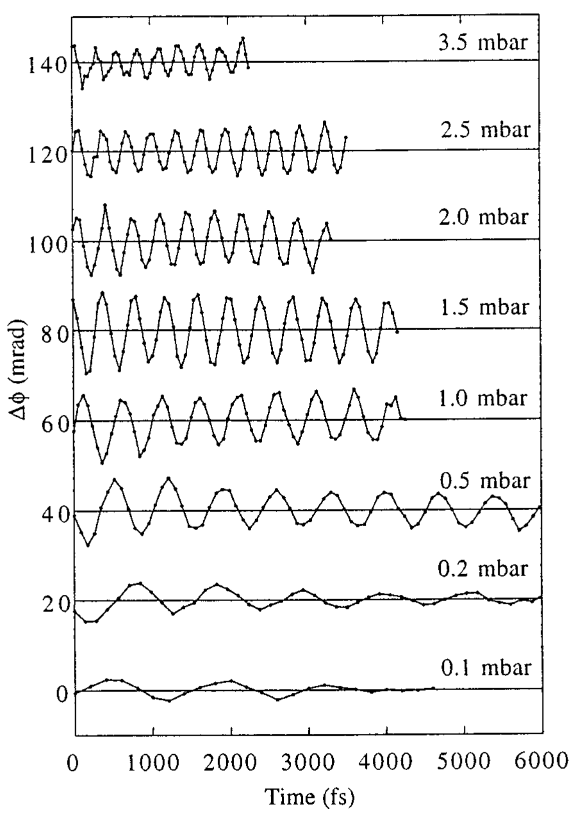

FIG. 8. Relative phase on the laser axis as a function of time for different helium gas pressures. Successive curves are incremented by 20 mrad.

B. LWF amplitude

The maximum relative phase $\Delta\phi_{\max}$ measured on the laser axis is plotted in Fig. 9 as a function of the electron density assuming a fully ionized He gas. This plot shows the LWF quasiresonance. The solid line is a fit using the expression of $\delta n_r = \delta n_{\max}(\omega_{pe}\tau_0)\exp[-2(\omega_{pe}\tau_0/2)^2]$ obtained from the linear theory (see Appendix A), where the adjustable parameters are an amplitude $\delta n_{\max}$ and the pump (and probe) pulse duration τ_0. The factor 2 in the exponential is due to the temporal convolution induced by the probe envelope: for a Gaussian envelope and a sinusoidal perturbation, the convolution decreases the phase shift by a factor of $\exp[-(\omega_{pe}\tau_1/2)^2]$, where τ_1 is the half width at $1/e$ in intensity of the probe pulse (see Appendix B). If we consider $\tau_1 = \tau_0$, the fit is obtained for $\tau_1 = \tau_0 = 84$ fs (FWHM$=140\pm 6$ fs) which is close to the laser pulse duration.

A more rigorous calculation must take into account the precise value of τ_1. The probe beam is first frequency doubled. This reduces the pulse length by a factor of $\sqrt{2}$. It then goes through several dispersive media: 2 cm of BK7 (Michelson cube), 1.4 cm of fused silica (dichroic mirror), and 6 mm of MgF_2 (chamber entrance window and focusing lens). Measurements of the pump spectrum show that the 120 ± 5 fs pulse is Fourier limited. From the frequency bandwidth, one can easily deduce that the duration of the probe pulses (FWHM) in the interaction chamber is 160 ± 5 fs. When the curve in Fig. 9 is fitted by the theoretical expression $\delta n_r = \delta n_{\max}(\omega_{pe}\tau_0)\exp[-2(\omega_{pe}\tau/2)^2]$ with the adjustable parameters $\delta n_{\max}$ and τ, we then have to compare $\tau = 84 \pm 4$ fs obtained from the fit with $\sqrt{(\tau_0^2+\tau_1^2)} = 85\pm 6$ fs.

A probe laser pulse that propagates through a thickness dz in an underdense plasma ($n_e/n_{cl} \ll 1$), undergoes a phase modification $d\phi = (2\pi/\lambda_1)(n_e(z)/2n_{cl})dz$, where λ_1 and n_{cl} are the probe wavelength and the corresponding critical density. The relationship between the measured relative phase shift and the maximum density perturbation at the focal plane is obtained by integration along the laser axis. The radial density oscillation $\delta n_r(z)$ is proportional to $1/\sigma^4(z)$, where $\sigma(z)$ is the radius of the intensity profile at $1/e$ at the

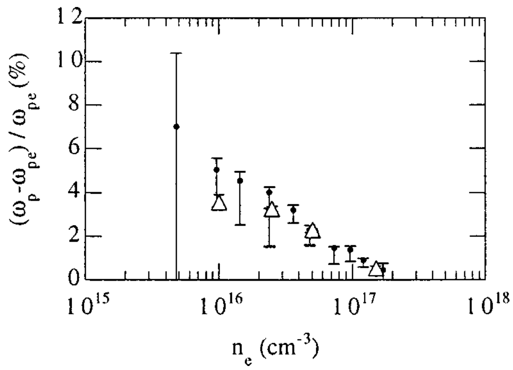

FIG. 10. Relative increase of the electron plasma frequency as a function of the electron density. Full circles: experimental results. Open triangles: simulations with the code WAKE.

position z along the laser axis. Assuming a Gaussian propagation and $z=0$ at the focal plane, then $\sigma(z)=\sigma\sqrt{(1+z^2/z_R^2)}$. Integration along z gives

$$\Delta\phi_{\max}=\pi^2\,\frac{\delta n_r(z=0)}{n_{c1}}\,\frac{z_R}{\lambda_1}\,e^{-(\omega_{pe}\tau_1/2)^2}.$$

The exponential term comes from the temporal convolution induced by the finite probe pulse duration (see Appendix A).

The product $z_R\delta n_r/n_e$ obtained from this formula is presented in Fig. 9. The solid line is a fit using the expression of $\delta n_r/n_e=B\exp[-C\omega_{pe}^2]/\omega_{pe}$, obtained from the linear theory (see Appendix A). In this experiment, z_R is estimated to be between 100 and 200 μm, so that the relative density perturbation at the focus is $\delta n_r/n_e\approx 10\%$ at the resonance density ($n_e\approx 10^{17}$ cm^{-3}) and reaches $\delta n_r/n_e\approx 100\%$ for $n_e\leqslant 10^{16}$ cm^{-3}. Let us underline that even when the density perturbation is nonlinear, the measured phase shift presented in Figs. 5–8 still has a sinusoidal temporal behavior and a smooth radial profile. This is due to two main reasons: with a time separation of 1.5 T_{pe} between the probe pulses, the measured phase corresponds to the peak-to-peak amplitude and that leads to a symmetric behavior around zero. Moreover, the maxima of a nonlinear density perturbation are very narrow in space and time. The temporal envelope of the probe pulses (see Appendix B) the finite spatial resolution of the imaging system, and the integration along the laser axis average these narrow peaks, as confirmed by simulations presented in Sec. IV C.

A calculation of the tunneling ionization rate of helium by the pump laser pulse indicates that the plasma should be singly ionized for $|z|\leqslant 7\,z_R$, and doubly ionized for $|z|\leqslant 2.5\,z_R$ on the laser axis. Therefore the phase amplitude ratio $\Delta\phi_{\rm abs}/\Delta\phi_{\rm rel}$ between the absolute and the relative mode measurements should be about 4 at low density ($n_e\leqslant 10^{16}$ cm^{-3}, where $\delta n_r/n_e\approx 1$) and proportional to $(\delta n_r/n_e)^{-1}$. This is in good agreement with our measurements.

C. Nonlinear frequency increase

The relative difference $(\omega_p-\omega_{pe})/\omega_{pe}$ between the measured frequency ω_p and the theoretical linear plasma frequency ω_{pe} is presented in Fig. 10 as a function of the electron density n_e. A positive shift (frequency higher than the theoretical linear frequency) can be clearly seen. It increases with decreasing electron density, and reaches 5% for $n_e\approx 10^{16}$ cm^{-3}. The results of the code WAKE originally developed by Mora and Antonsen, Jr.[21] are represented by open triangles. This code is a two-dimensional (2-D) (cylindrical), fully relativistic particle code, in which the laser field acts on the particles via the ponderomotive force. The new version of the code used here also simulates the plasma formation by tunneling ionization (via a Monte Carlo method), the propagation of the two frequency doubled probe pulses, the imaging lens, and the time domain interferometry (see Appendix C). To simulate the kinetic energy produced during the ionization, the electrons can be generated with a Maxwellian radial velocity distribution. The plasma frequency increase obtained from the code is in good agreement with the measurements. As we have noted for the experimental results in Sec. IV B, even when the density perturbation is nonlinear, the code shows that the measured phase shift has a sinusoidal time evolution and a radial profile very similar to the one obtained from linear theory. Applying the same fit $(\Delta\phi_{\max}*\exp[-\gamma(t-t_0)]*\sin[\omega_p(t-t_0)])$ to much later periods (when the EPW relative amplitude is smaller) shows that the shift disappears, both in the experiment and in the simulations. This indicates that the shift does not come from an error in the pressure measurement or from the delay-line calibration, but is related to the nonlinear amplitude of the EPW.

Few mechanisms can modify the electron plasma frequency. In a hot plasma the frequency increases with the electron temperature: $\omega_p^2=\omega_{pe}^2+3k^2v_{th}^2$. The transverse residual energy produced by a linearly polarized laser pulse ionizing a helium gas can be calculated using the tunneling ionization rate.[19,22,23] It is of the order of 60 eV for our experimental conditions. The code WAKE shows that the electron temperature does not affect the plasma frequency so much: changing the temperature from 0 to 50 eV leads to a positive frequency shift of a few 10^{-3}, that is ten times less than the measured shift. In addition, the shift disappears after a few periods (≈ 1 ps), and we do not think that the electron temperature can vanish in such a short time scale. So this effect is not related to the electron temperature. The plasma period can also be modified when the electrons of the EPW reach relativistic velocities.[24] This shift has recently been observed by Modena *et al.* in SRLWF.[25] The increase of the electron relativistic factor γ induces a decrease of the frequency (negative shift). Our simulation shows that the velocity of the electrons does not exceed $v/c\approx 0.1$ (at $n_e=10^{16}$ cm^{-3}) and that leads to a shift of only -0.25%.

For oscillations in a 3-D space, two other effects induce a frequency modification. (a) When electrons execute an elliptic motion, current loops and magnetic fields are produced.[26,27] The magnetic field deflects electron motion to the third order in amplitude and that induces a decrease of the electron plasma frequency. (b) In the case of nonlinear cylindrical electrostatic oscillations, the radial displacement of an electron away from the symmetry axis produces a charge density at the center which is greater than in planar geometry. This produces a stronger restoring electric field and leads to an increase (positive shift) of the electron plasma frequency $[\Delta\omega_p/\omega_{pe} \approx (\delta r/r_0)^2/12$, where δr is the electron displacement from its initial position r_0, and $\delta r/r_0 \ll 1]$.[17]

The total frequency shift depends on the relative amplitude of the thermal, the relativistic, the electrostatic, and the magnetic effects, or, in other words, on the geometry and amplitude of the oscillation. In the context of the laser beat-wave accelerator, Bell and Gibbon[26] have shown that these effects can have similar amplitudes and comparable spatial profiles. The code WAKE includes all these effects. Measurements and simulations both indicate that the electrostatic effect (frequency increase) is predominant in this experiment. It is to our knowledge the first observation of this effect that was predicted by Dawson in 1959.[17]

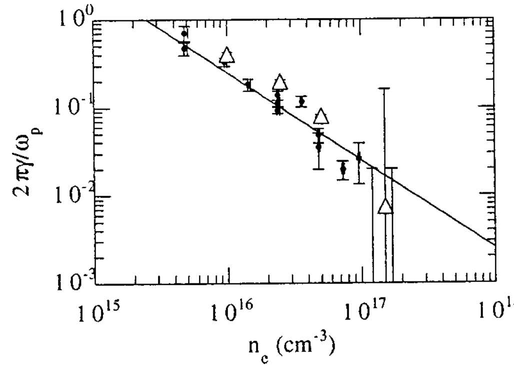

FIG. 11. Damping rate of the electron oscillation versus the electron density. The open triangles are the results of the code WAKE. The solid line is a A/n_e fit.

D. Damping of the oscillations

We have obtained the value of the damping rate γ from the fit of Fig. 8 in Sec. IV A. The dependence of γ as a function of the mean electron density n_e is shown in Fig. 11, together with the values obtained by simulations (open triangles). At high electron densities ($>10^{17}$ cm^{-3}), the damping is very slow (tens of periods): due to the limited time range we have used, the relative uncertainty of these low values of γ is large. When the density is lower ($<10^{16}$ cm^{-3}), the oscillation is damped in two or three periods only. The solid line is a fit of the form A/n_e that shows that γ/ω_{pe} is approximately inversely proportional to the electron density.

This damping cannot be the signature of the ion motion. Indeed, the ion plasma frequency is 60 times lower than the electron plasma frequency for a fully ionized helium plasma. So the typical time of the damping induced by the ion motion expressed in plasma period units is about 60 and is independent of the electron mean density.

Several mechanisms can attenuate the oscillation. One of them is the fine scale mixing:[17] the frequency of the oscillation depends on its relative amplitude. Electrons with different equilibrium radii have different frequencies. After some time, crossings of electrons can occur and induce a damping. With a maximum frequency shift of 5% at $n_e = 10^{16}$ cm^{-3}, electrons should appear with opposite phases after at least ten periods, which is five times longer than the observed damping rate. Another possible mechanism is the thermal convection: The density perturbation propagates at the group velocity $v_g = \partial\omega/\partial k$, where $\omega^2 = \omega_{pe}^2 + 3k^2 v_{th}^2$. Simulations made in a preionized homogeneous plasma show a much slower attenuation (ten times slower than experimental re-

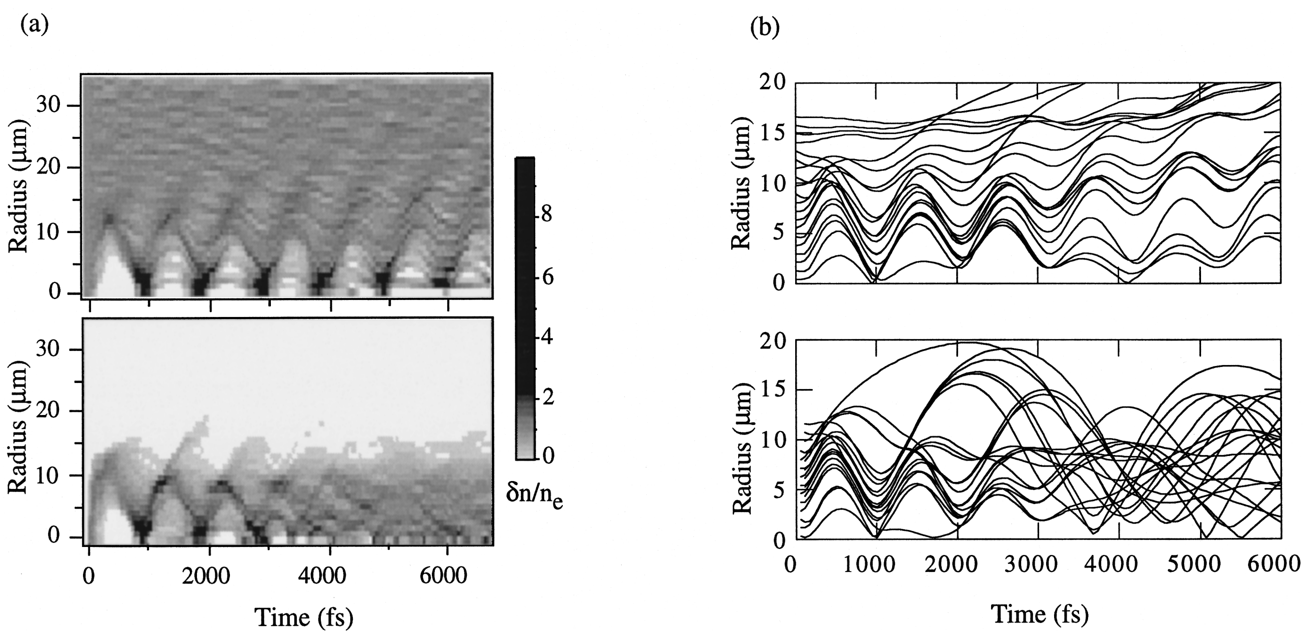

FIG. 12. (a) Electron density at the laser focus as a function of radius and time obtained from the code WAKE. Bottom graph: tunneling ionized helium plasma with $n_{\mathrm{atom}} = 5\times10^{15}$ cm^{-3}. Top graph: preionized homogeneous fully ionized helium plasma with $n_e = 10^{16}$ cm^{-3} and $T_e = 50$ eV. (b) Radial electron trajectories at the focal plane versus time corresponding to (a). Bottom graph: tunneling ionized helium gas. Top graph: preionized homogeneous fully ionized helium plasma.

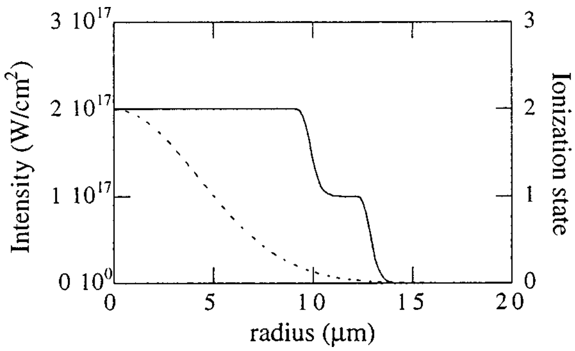

FIG. 13. Solid line: ionization state calculated as a function of the radius. Dashed line: laser intensity profile used to calculate the ionization.

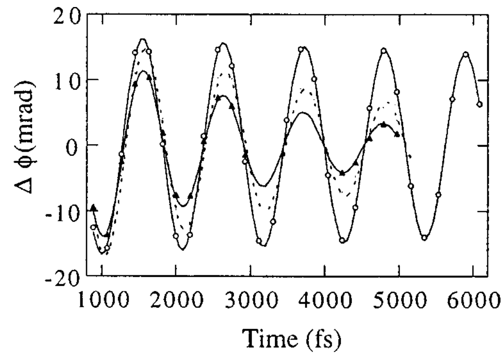

FIG. 14. Relative phase shift on the laser axis obtained from the code WAKE in the conditions of Figs. 12(a) and 12(b). Solid line with open circles: preionized plasma with $T_e = 50$ eV. Solid line with full triangles: tunneling ionized gas with $T_e = 50$ eV. Dotted line: tunneling ionized gas with $T_e = 0$ eV.

sults at 10^{16} cm^{-3}), indicating that neither the convection nor the fine scale mixing can explain the observed damping rate.

A good agreement is only obtained by taking into account the gas ionization as we have done in the simulations in Fig. 11. Two simulations at $n_e = 10^{16}$ cm^{-3} are presented in Fig. 12(a), one in a preformed homogeneous plasma (top graph), and the other in a tunneled-ionized helium gas (bottom graph). They show the electron density at the laser focal plane as a function of the radius (vertical axis) and time (horizontal axis). One can see the electron density oscillation around the laser axis. In the case of the tunneling ionized helium gas, the plasma exists only in a small region near the laser axis ($r < 15$ μm).

The radial profiles of the laser intensity and of the calculated electron density at the laser focal plane are shown in Fig. 13. One can see the two steep density gradients corresponding to the two ionization stages of helium. The fully ionized helium plasma has a radial extent of only 10 μm.

The electron radial positions at the laser focal plane are presented in Fig. 12(b) as a function of time. At time$=0$, the electrons begin to feel the ponderomotive force of the pump laser pulse and move away from focus. After the laser pulse, the electrons are pulled back by the electrostatic field and they oscillate at the plasma frequency. In the homogeneous plasma, this oscillation decreases quietly with time. In the case of a plasma created by tunneling ionization, the radial density profile of the plasma modifies the electron trajectories: when it is pushed by the ponderomotive force of the laser pulse, an electron close to the He^{2+}/He^{+} interface can explore the He^{+} region or even the neutral gas. In these regions, the electrons do not follow the collective motion of the EPW, they come back into the plasma after a few oscillations of the EPW. These electrons are not in phase with the EPW and destroy the oscillation.

This phenomenon can be understood as follows. In a preformed plasma radially larger than the perturbation, when an corona electron moves away from the laser axis, a positive charge is created. This induces a restoring electrostatic force which is proportional to the electron displacement: it is an harmonic oscillator at the electron plasma frequency. In the case of a radially limited plasma, when the corona electron leaves the plasma, the number of positive charges is fixed by the plasma radius. This induces a lower restoring force and explains why the electrons come back in the plasma later than in the case of an infinite plasma.

A simulation of the relative phase shift oscillation in the conditions of Figs. 12(a) and 12(b) is presented in Fig. 14. One can see the sinusoidal behavior of the phase shift and the damping. We also added a curve corresponding to an ionization without heating ($T_e = 0$). In that case the damping is a little bit slower than when $T_e = 50$ eV (two times slower at 10^{16} cm^{-3}) but still remains much faster than in a preformed plasma.

A similar plasma edge effect has been observed in particle-in-cell (PIC) simulations by Bonnaud *et al.*[28] in the case of an EPW excited in a planar geometry (longitudinal LWF) and in a cold plasma. This damping mechanism is more important at low density because the electron excursion increases with $\delta n_r / n_e$ which is larger at low density (cf. Fig. 9).

V. CONCLUSION

We have performed the first detailed experimental study of the electron density oscillation produced in the wake of a laser pulse. The electron oscillation is measured with a time resolution much better than the electron plasma period, and a spatial resolution smaller than the pump focal spot radius. The spatial shape and size of the perturbation agree with the laser wakefield linear theory. The laser wakefield quasiresonance is observed. Depending on the background electron density, the relative density perturbation amplitude is between a few percent and 100%. In the density range of our experiment, the damping rate normalized to the plasma frequency varies approximately linearly with the radial relative electron density perturbation. The damping time goes from two periods at 5×10^{15} cm^{-3} (nonlinear oscillation amplitude) to tens of periods for densities above 10^{17} cm^{-3} (linear amplitude). The simulations show that because the oscillation is radial, electrons exit from the plasma and lead to the destruction of the plasma oscillation. In the nonlinear regime, the electron plasma frequency increases, as predicted by Dawson in 1959[17] for radial (cylindrical) oscillations.

ACKNOWLEDGMENTS

It is a pleasure to acknowledge the help from G. Hammoniaux, G. Grillon, and G. Rey. This work has been supported by the Centre National de la Recherche Scientifique and by the European Union large facility program under the Contract No. CHGE CT930021.

APPENDIX A: LASER WAKEFIELD LINEAR THEORY

A two-dimensional, nonrelativistic, analytical model of the LWF process has been developed by Gorbunov and Kirsanov.[12] The electron motion is calculated by solving the linear fluid equations:

$$\frac{\partial \delta n}{\partial t} + n_e \nabla \cdot \mathbf{v} = 0,$$

$$m_e \frac{\partial \mathbf{v}}{\partial t} = -e\mathbf{E} + e\nabla \phi_{\mathrm{NL}},$$

$$\nabla \cdot \mathbf{E} = -\frac{e}{\epsilon_0}\,\delta n,$$

where the electric field $\mathbf{E}$ is related to the potential ϕ by $\mathbf{E} = -\nabla \phi$, and where m_e, e, and v are the electron mass, charge, and velocity, ϵ_0 is the vacuum permittivity, n_e is the electron density at equilibrium, δn is the electron perturbation ($\delta n \ll n_e$), and ϕ_{NL} the ponderomotive potential associated to the laser pulse:

$$\phi_{\mathrm{NL}} = -\frac{m_e}{e}\frac{\langle v_{\mathrm{osc}}^2\rangle}{2},$$

which is equivalent to

$$\phi_{\mathrm{NL}} = -\frac{I}{2ecn_c}$$

(v_{osc} is the quiver velocity in the laser field, $\langle\,\rangle$ denotes a temporal average on a laser period, I is the laser intensity, and n_c the critical density at the laser wavelength). Because we are interested in time scales of the order of the electron plasma period, the ions can be assumed to be fixed. The evolution of the potential is obtained by combining these equations:

$$\left(\frac{\partial^2}{\partial t^2} + \omega_{pe}^2\right)\phi = -\omega_{pe}^2 \phi_{\mathrm{NL}}, \tag{A1}$$

where ω_{pe} is the electron plasma frequency: $\omega_{pe}^2 = n_e e^2/m_e\epsilon_0$.

This equation can be solved in a cylindrical geometry assuming that the radial (r) and the temporal ($z-ct$) part of the ponderomotive potential can be separated:

$$\phi_{\mathrm{NL}}(r,z,t) = \phi_0(r) f_0(z-ct).$$

This implies

$$\phi(r,z,t) = \phi_0(r) f(z-ct).$$

In the dimensionless form, Eq. (A1) becomes

$$\left(\frac{\partial^2}{\partial \tau^2} + 1\right) f(\tau) = -f_0(\tau), \tag{A2}$$

where $\tau = \omega_{pe}(t - z/c)$.

The solution that cancels at $\tau = -\infty$ is

$$f(\tau) = -\int_{-\infty}^{\tau} f_0(\tau')\sin(\tau-\tau')\,d\tau',$$

or

$$f(\tau) = \cos(\tau)\int_{-\infty}^{\tau} f_0(\tau')\sin(\tau')\,d\tau' - \sin(\tau)\int_{-\infty}^{\tau} f_0(\tau')\cos(\tau')\,d\tau'.$$

In the laser pulse wake ($\tau \gg 1$), and if f_0 is an even function, this solution is

$$f(\tau) = -\sin(\tau)\int_{-\infty}^{+\infty} f_0(\tau')\cos(\tau')\,d\tau'.$$

In the case of a laser pulse with a Gaussian temporal profile, $f_0(\tau) = -\exp(-\tau^2/(\omega_{pe}\tau_0)^2)$, we get

$$f(\tau) = \sqrt{\pi}(\omega_{pe}\tau_0)\exp\left(-\frac{(\omega_{pe}\tau_0)^2}{4}\right)\sin(\tau).$$

If the radial envelope is also Gaussian: $\phi_0(r) = (m_e c^2/2e) \times \langle v_{\mathrm{osc}}^2/c^2\rangle_{\max}\exp(-r^2/\sigma^2)$, the potential in the laser pulse wake is (in real dimensions)

$$\phi(r,z,t) = \varphi\, \exp\left(-\frac{r^2}{\sigma^2}\right)\sin(\omega_{pe}t - k_p z) \tag{A3}$$

with

$$\varphi = \sqrt{\pi}\,\frac{m_e c^2}{e}\left\langle\frac{v_{\mathrm{osc}}^2}{c^2}\right\rangle_{\max}\left(\frac{\omega_{pe}\tau_0}{2}\right)\exp\left[-\left(\frac{\omega_{pe}\tau_0}{2}\right)^2\right],$$

or

$$\varphi = \sqrt{\pi}\,\frac{I_{\max}}{ecn_c}\left(\frac{\omega_{pe}\tau_0}{2}\right)\exp\left[-\left(\frac{\omega_{pe}\tau_0}{2}\right)^2\right].$$

The electric field can be obtained from $\mathbf{E} = -\nabla\phi$, and the electron density perturbation from the Poisson law: $\delta n = (\epsilon_0/e)\Delta\phi$, or

$$\delta n = \frac{\epsilon_0}{e}\left(\frac{\partial^2}{\partial z^2} + \frac{1}{r}\frac{\partial}{\partial r}\, r\, \frac{\partial}{\partial r}\right)\phi.$$

The electron density perturbation is the sum of two terms: $\delta n = \delta n_z + \delta n_r$. The first one δn_z comes from the longitudinal oscillation of the electrons induced by the temporal profile of the laser pulse, while the second one δn_r corresponds to the transverse motion induced by the radial profile of the pulse.

$$\frac{\delta n}{n_e} = A\left[1 + \left(\frac{2c}{\omega_{pe}\sigma}\right)^2\left(1 - \frac{r^2}{\sigma^2}\right)\right]\exp\left(-\frac{r^2}{\sigma^2}\right) \times \sin(\omega_{pe}(t - z/c)), \tag{A4}$$

where

$$A = \frac{I\sqrt{\pi}}{c^3 n_c m_e}\left(\frac{\omega_{pe}\tau_0}{2}\right)\exp\left[-\left(\frac{\omega_{pe}\tau_0}{2}\right)^2\right]$$

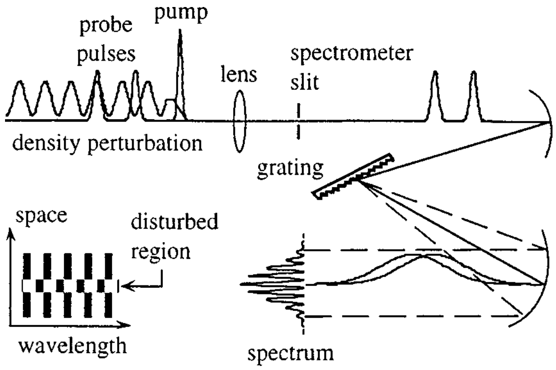

FIG. 15. The frequency-domain interferometry setup.

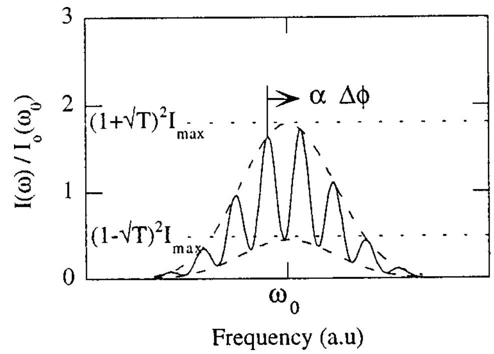

FIG. 16. Solid line: typical spectrum of the frequency-domain interferometry.

or

$$A \cong 21 P(TW)\left(\frac{\lambda}{\sigma}\right)^2\left(\frac{\omega_{pe}\tau_0}{2}\right)\exp\left[-\left(\frac{\omega_{pe}\tau_0}{2}\right)^2\right].$$

APPENDIX B: THE FREQUENCY DOMAIN INTERFEROMETRY

1. Principle

Tokunaga *et al.*[29] have demonstrated that the spectral interference of two twin ultrashort laser pulses can be used to measure the temporal evolution of the refractive index of an excited absorptive material. Geindre *et al.*[20] added to this technique a one-dimensional spatial resolution and measured the expansion of the critical density surface of a femtosecond laser-produced plasma with subnanometer spatial resolution and a sub-100 fs temporal resolution. Temporal[15] and spatiotemporal[13,16] measurements of the electron density oscillation produced by the laser wakefield process has been performed with this technique. The principle of this frequency-domain interferometry of ultrashort laser pulses is the following.

In the new method that we have developed, two collinear identical laser pulses, overlapped in space, are created by sending a low-intensity short laser pulse in a Michelson interferometer. The output pulses are separated by δt, follow exactly the same path, and irradiate the object to be studied. The perturbation of the object can be done before the arrival of the twin pulses, or between them, for example, by the interaction with a high-intensity laser pulse. The interaction with the object modifies the relative phase of the twin pulses. After the interaction, the two pulses are sent in a spectrometer. By dispersing the pulse spectrum, the grating also temporally stretches the two pulses, which makes them overlap in time. Their temporal beating creates interference fringes in the frequency domain. The position of these fringes depends on the relative phase between the pulses. The interaction region is imaged on the vertical entrance slit of the spectrometer. The spectrum and so the relative phase are then spatially resolved along the slit axis (cf. Fig. 15). Let us note that because the object is irradiated by the far field of the probe beam, relative phase shifts produced by defects on the Michelson mirrors (near field) are smoothed at the object plane.

2. Theory

Let us consider a point along the entrance slit of the spectrometer which is the image of a point of the object to the studied. The electric field associated to the twin pulses can be expressed by

$$E_1(t)=E_0(t)e^{i\omega_0 t} \quad \text{(first pulse)},$$

$$E_2(t)=E_0(t-\delta t)e^{i\omega_0(t-\delta t)}\sqrt{T(t-\delta t)}e^{i\Delta\phi(t-\delta t)}$$
$$\text{(second pulse)},$$

where ω_0 is the laser pulse frequency, and where we have supposed that during the interaction, the probe pulse has undergone a phase shift $\Delta\phi$ and an intensity decrease characterized by the transmission coefficient T. The frequency spectrum in intensity is obtained by the Fourier transform of the total electric field:

$$I(\omega)=\frac{\epsilon_0 c}{2}\,|TF(E_1(t)+E_2(t))|^2.$$

If the transmission coefficient T and the phase shift $\Delta\phi$ do not evolve during the laser pulse, the intensity spectrum is

$$I(\omega)=I_0(\omega)[1+T+2\sqrt{T}\cos(\omega\delta t-\Delta\phi)],$$

where

$$I_0(\omega)=\frac{\epsilon_0 c}{2}\,|E_0(\omega-\omega_0)|^2.$$

The spectrum of the twin pulses has an envelope that is identical to the spectrum $I_0(\omega)$ of a single probe pulse, but modulated by a cosine function (cf. Fig. 16). The fringes are separated in frequency by $2\pi/\delta t$, so that the larger is δt, the more fringes are present in the spectrum. Their contrast depends on the transmission coefficient T, and is maximum for $T=1$. One can obtain simultaneously the transmission coefficient from the contrast of the spectrum and the relative phase shift from the displacement of the system of fringes.

What makes this diagnostic very performable is that each point along the spectrometer slit corresponds to a complete system of fringes along the dispersion axis. The signal-to-noise ratio is then strongly increased (proportional to the number of points along a line of the detector), and the results are largely insensitive to the local defects of the detector.

The phase information is extracted from the spectral domain by calculating the inverse Fourier transform of $I(\omega)$. In the general case, one has

$$FT^{-1}[|FT(E_1(t)+E_2(t))|^2] = E_1(t)\otimes E_1^*(-t)+E_2(t)\otimes E_2^*(-t) + E_1(t)\otimes E_2^*(-t)+E_2(t)\otimes E_1^*(-t),$$

where $\otimes$ is the convolution product.

Let us note $G(t')=(\epsilon_0 c/2)\int_{-\infty}^{+\infty}E_0(t)E_0^*(t-t')dt$. This autocorrelation function is centered at $t'=0$ and has a width of the order of the probe pulse duration τ_1.

If T and $\Delta\phi$ are time independent, then

$$FT^{-1}[I(\omega)](t')=(1+T)G(t')e^{i\omega_0 t'} + \sqrt{T}[G(t'+\delta t)e^{i\omega_0(t'+\delta t)}e^{-i\Delta\phi} + G(t'-\delta t)e^{i\omega_0(t'-\delta t)}e^{i\Delta\phi}].$$

Taking the inverse Fourier transform equal at the time $t'=\delta t$, one gets

$$FT^{-1}[I(\omega)](\delta t)=(1+T)G(\delta t)e^{i\omega_0\delta t} + \sqrt{T}G(2\delta t)e^{i2\omega_0\delta t}e^{i\Delta\phi} + \sqrt{T}G(0)e^{i\Delta\phi}.$$

If the probe pulse duration τ_1 is much smaller than the probe pulses separation ($\tau_1\ll\delta t$), the dominant term is $G(0)=(\epsilon_0 c/2)\int_{-\infty}^{+\infty}|E_0(t)|^2dt$ which is the integral (real) of the reference pulse intensity. The phase $\phi_m(\delta t)$ at $t=\delta t$ of the inverse Fourier transform of the spectrum in intensity is then:

$$\phi_m(\delta t)=\arctan\left[\frac{\mathrm{Im}\{TF^{-1}[I(\omega)](\delta t)\}}{\mathrm{Re}\{TF^{-1}[I(\omega)](\delta t)\}}\right]\approx\Delta\phi.$$

If $\Delta\phi$ and T vary in the laser pulse temporal envelope, then the dominant term at $t'=\delta t$ is

$$FT^{-1}[I(\omega)](\delta t)\approx\int_{-\infty}^{+\infty}I_0(t)\sqrt{T(t)}e^{i\Delta\phi(t)}dt,$$

where $I_0(t)=E_0(t)E_0^*(t)$.

One then gets

$$\phi_m(\delta t)\approx\arctan\left[\frac{\int_{-\infty}^{+\infty}I_0(t)\sqrt{T(t)}\,\sin[\Delta\phi(t)]dt}{\int_{-\infty}^{+\infty}I_0(t)\sqrt{T(t)}\,\cos[\Delta\phi(t)]dt}\right].$$

For a small phase shift ($\Delta\phi\ll 1$),

$$\phi_m(\delta t)\approx\frac{\int_{-\infty}^{+\infty}I_0(t)\sqrt{T(t)}\Delta\phi(t)dt}{\int_{-\infty}^{+\infty}I_0(t)\sqrt{T(t)}dt}.$$

If the two probe pulses are temporal Dirac functions, then the measured phase is exactly the relative phase $\Delta\phi(t)$. The finite duration of the pulses induces a smoothing of the information: the measured phase $\phi_m(\delta t)$ is the temporal average of the phase shift $\Delta\phi(t)$ weighted by the intensities of the pulses $I_0(t)$. In the case of Gaussian laser pulses $[I_0(t)=I_{\max}\exp(-(t/\tau_1)^2)]$ in an electron plasma wave $[\Delta\phi(t)=\Delta\phi_{\max}\sin(\omega_{pe}t)]$, and assuming $T(t)\approx 1$, the measured phase is $\phi_m(\delta t)\approx\Delta\phi_{\max}\exp(-(\omega_{pe}\tau_1/2)^2)$.

3. Error on the measured relative phase

Let us estimate the phase error made by neglecting the terms $G(\delta t)$ and $G(2\delta t)$:

$$\mathrm{Im}\{\mathrm{Ln}[FT^{-1}[I(\omega)](\delta t)]\}=\Delta\phi+\mathrm{Im}\{\mathrm{Ln}[1+u]\},$$

where

$$u=\frac{(1+T)G(\delta t)e^{i\omega_0\delta t}}{\sqrt{T}G(0)e^{i\Delta\phi}}+\frac{G(2\delta t)e^{2i\omega_0\delta t}}{G(0)e^{2i\Delta\phi}}.$$

Assuming $u\ll 1$, one gets

$$\phi_m(\delta t)\approx\Delta\phi+\mathrm{Im}\left\{\frac{(1+T)G(\delta t)}{\sqrt{T}G(0)}\,e^{i(\omega_0\delta t-\Delta\phi)} + \frac{G(2\delta t)}{G(0)}\,e^{2i(\omega_0\delta t-\Delta\phi)}\right\},$$

which gives for a small phase shift

$$\phi_m(\delta t)\approx\Delta\phi+\left[\frac{(1+T)G(\delta t)}{\sqrt{T}G(0)}\sin\omega_0\delta t + \frac{G(2\delta t)}{G(0)}\sin 2\omega_0\delta t\right] - \Delta\phi\left[\frac{(1+T)G(\delta t)}{\sqrt{T}G(0)}\cos\omega_0\delta t + 2\frac{G(2\delta t)}{G(0)}\cos 2\omega_0\delta t\right].$$

An advantage of having a spatial resolution is that the phase shift is obtained by subtracting from the phase measured in a perturbed region (around the laser axis), the phase of an unperturbed region (far from the laser axis). In that case, the second term of the above expression is subtracted, and one gets:

$$\phi_m(\delta t)\approx\Delta\phi\left[1-\frac{(1+T)G(\delta t)}{\sqrt{T}G(0)}\cos\omega_0\delta t - 2\frac{G(2\delta t)}{G(0)}\cos 2\omega_0\delta t\right].$$

In the case of a Gaussian laser pulse, $E_0(t)=E_{\max}\times\exp(-(t/\tau_1)^2/2)$, one gets

$$\phi_m(\delta t)\approx\Delta\phi\left[1-\frac{1+T}{\sqrt{T}}\,e^{-1/4(\delta t/\tau_1)^2}\cos\omega_0\delta t - 2e^{-(\delta t/\tau_1)^2}\cos 2\omega_0\delta t\right].$$

For $T=1$, the maximum relative error on the phase is smaller than 1% for $\delta t\approx 3\tau_1$. In the experiment presented in this article, the pulse separation was adjusted to $\delta t=1.5T_{pe}$. The pulse duration was $\tau_1\approx 95$ fs, so that the phase relative error was smaller than 5% for $n_e\leqslant 2\times 10^{17}$ cm^{-3}, which was always the case.

A more realistic calculation taking into account the time dependence of $\Delta\phi$ and the limited width of the recorded spectrum (CCD chip size) increases this relative error to less than 15% for $n_e \leqslant 2\times10^{17}\ \mathrm{cm}^{-3}$. So, in our case, these effects are not limitative at all.

4. Noise sources on the measurement of the relative phase

The shot-to-shot fluctuations of the spectrum recorded on the CCD and of δt can induce a phase error. If we assume that the pulse spectrum does not depend on the position in the beam, then we can take the reference in a nonperturbed region of the probe beam and these errors are eliminated. This is an other advantage of having a spatial resolution.

Anyway, each measure is obtained from the averaged spectrum of 40 shots. This procedure reduces drastically the stochastic noise coming from the laser fluctuations. We have measured the rms of this noise: it is around 5 mrad without averaging, and it decreases to 0.5 to 1 mrad with a 40 shot averaging. In fact, the rms is yet at this value when we operate only a 20 or a 30 shot averaging. Consequently, there is another noise source which prevents us from improving our signal-to-noise ratio.

The second noise source is the detector (CCD) noise. At each position on the spectrometer slit, the detected signal $S(\omega)$ is the laser signal $I(\omega)$ plus a background noise $B(\omega)$, so that

$$\mathrm{Im}\{\ln(FT^{-1}[S(\omega)](\delta t))\} = \phi_m + \mathrm{Im}\left\{\ln\left(1+\frac{FT^{-1}[B(\omega)](\delta t)}{FT^{-1}[I(\omega)](\delta t)}\right)\right\}.$$

If the CCD noise is much smaller than the laser signal, and assuming $\phi_m \approx \Delta\phi$, the detected phase ϕ_d is

$$\phi_d \approx \Delta\phi + \mathrm{Im}\left\{\frac{FT^{-1}[B(\omega)](\delta t)}{FT^{-1}[I(\omega)](\delta t)}\right\}$$

or

$$\phi_d \approx \Delta\phi + \frac{1}{\sqrt{T}G(0)}\int_{-\infty}^{+\infty} B(\omega)\sin(\omega\delta t-\Delta\phi)\,d\omega.$$

Experimentally, the signal is sampled on the N pixels of the CCD camera. Let us note $\delta\omega$ the frequency step of the sampling, the inverse Fourier transform is then

$$\phi_d \approx \Delta\phi + \frac{1}{\sqrt{T}G(0)}\ \delta\omega \sum_{m=-N/2}^{N/2} B(m\,\delta\omega)\sin(m\,\delta\omega\,\delta t-\Delta\phi).$$

If we note $\sigma(\Delta\phi)$ the standard deviation of the phase, $\sigma^2(\Delta\phi) = \langle(\Delta\phi-\phi_d)^2\rangle$, we have

$$\sigma^2(\Delta\phi) = \left(\frac{1}{\sqrt{T}G(0)}\right)^2 \times \left\langle\left(\delta\omega \sum_{m=-N/2}^{N/2} B(m\,\delta\omega)\sin(m\,\delta\omega\,\delta t-\Delta\phi)\right)^2\right\rangle.$$

The detector noise can be written as $B = B_{\mathrm{av}} + \delta B$. The average noise B_{av} has been measured on the CCD without laser signal: it is the same for all the pixels. The stochastic variable δB satisfies $\langle\delta B\rangle = 0$. This leads to

$$\sigma^2(\Delta\phi) = \left(\frac{1}{\sqrt{T}G(0)}\right)^2 \times \left\langle\left(\delta\omega \sum_{m=-N/2}^{N/2} \delta B(m\,\delta\omega)\sin(m\,\delta\omega\,\delta t-\Delta\phi)\right)^2\right\rangle.$$

If we assume that the pixels are not correlated and that the noise does not depend on the signal on the pixel, then

$$\sigma^2(\Delta\phi) = \left(\frac{\delta\omega}{\sqrt{T}G(0)}\right)^2 \times \left\langle \sum_{m=-N/2}^{N/2} \delta B^2(m\,\delta\omega)\sin^2(m\,\delta\omega\,\delta t-\Delta\phi)\right\rangle,$$

$$\sigma^2(\Delta\Phi) = \left(\frac{\delta\omega}{\sqrt{T}G(0)}\right)^2 \frac{1}{2}\left\langle \sum_{m=-N/2}^{N/2} \delta B^2(m\,\delta\omega)\right\rangle,$$

$$\sigma^2(\Delta\phi) = \left(\frac{\delta\omega}{\sqrt{T}G(0)}\right)^2 \frac{N}{2}\langle\delta B^2(\omega)\rangle.$$

Using the fact that

$$G(0) \approx \delta\omega \sum_{m=-N/2}^{N/2} I(m\,\delta\omega) = \delta\omega N I_{\mathrm{av}}$$

we finally get

$$\sigma(\Delta\phi) = \frac{1}{\sqrt{2NT}}\frac{\sigma(B)}{I_{\mathrm{av}}},$$

where $\sigma^2(B) = \langle(B-B_{\mathrm{av}})^2\rangle$.

This phase noise can be decreased by working close to the saturation of a high-dynamic CCD camera (I_{av}) and with a large number of pixels (N). It does not depend on the number of fringes. With our 16 bits CCD camera, $N=512$, $\sigma(B)\approx 7$ counts. The average signal is around 2×10^4 counts, so that the phase noise coming from the camera is of the order of 10^{-2} mrad, indicating that the measured noise (of the order of 0.5 to 1 mrad) is not coming from the detector.

Another source of phase noise is coming from the defects of the spectrometer slit. This one is imaged on the frequency plane (CCD chip). Each point of the slit corresponds to a system of fringes. If the slit is not quite vertically straight, the fringes are not straight either. A horizontal defect δx on the slit induces a translation of the system of fringes, which gives the same result as a phase shift $\delta\phi$:

$$\delta\phi = \left[\left(\frac{d\omega}{dx}\right)\delta x\right]\delta t,$$

where $d\omega/dx$ is the frequency dispersion of the spectrometer. This phase noise increases with δt which means with the number of fringes. This dependence on the number of fringes is confirmed by our measurements of the noise rms with different δt. In our experiment, $d\omega/dx \approx 4.1 \times 10^{12}$ rad s^{-1} mm^{-1}. With $\delta t = 750$ fs (corresponding to an electron density $n_e = 5 \times 10^{16}$ cm^{-3}) and $\delta x = 1$ μm, one gets $\delta\phi \approx 3$ mrad.

Our measurements are made without changing δt. If the slit does not move, the systematic phase noise coming from the slit defect is the same from shot-to-shot and can then be eliminated by making a reference shot. The method we use keeps contributions from the vibration of the slit: high-frequency vibrations (>1 Hz) coming from the vacuum pump system are smoothed by the 40 shot (4 s.) averaging, but low-frequency position shifts of the slit are not eliminated and contribute to the background noise.

A modification $\Delta(\delta t)$ of δt is equivalent to a phase modification $\delta\phi = \omega_0 \Delta(\delta t)$. In our experiment $\omega_0 = 4.7 \times 10^{15}$ rad s^{-1}, so that a variation of 1.3 fs on δt is equivalent to a phase shift of 2π. However, the spatial resolution along one direction allows us to get rid of it: the calculated phase shift is obtained for each CCD image recorded by comparison with a reference line on the CCD (unperturbed fringes).

The number of photons N_{ph} follows a Poisson distribution so that its standard deviation on the CCD camera is $\sigma(N_{\mathrm{ph}}) = \sqrt{N_{\mathrm{ph}}}$. The ratio between N_{ph} and our corresponding CCD counts is of 6 photons (at 0.4 μm) for 1 CCD count. If we express $I(\omega)$ in CCD count units, then the photonic noise on each pixel is $\sigma_{\mathrm{ph}}(I) = (1/\sqrt{6})\ \sqrt{I}$. Assuming noncorrelated pixels, this photonic noise leads to the following phase standard deviation:

$$\sigma_{\mathrm{ph}}^2(\Delta\phi) = \frac{1}{6}\left(\frac{\delta\omega}{\sqrt{TG(0)}}\right)^2 \sum_{m=-N/2}^{N/2} I(m\,\delta\omega)\sin^2(m\,\delta\omega\,\delta t - \Delta\phi).$$

As the square of the sinus function is overestimated by 1, one can easily deduce that

$$\sigma_{\mathrm{ph}}(\Delta\phi) \leqslant \frac{1}{\sqrt{6TNI_{\mathrm{av}}}}.$$

With our experimental parameters, this noise is lower than 0.1 mrad and is not so limitative. This photonic noise can be reduced by increasing the number of probe photons on the CCD.

5. Conclusion

This diagnostic allows one to detect phase shifts with on-live spatial resolution, and with a precision under the mrad. The main limitation of this detection seems to come from the spatial quality of the spectrometer slit, and from the control of its vibrations.

APPENDIX C: THE CODES WAKE AND IMAGE

The simulations we show this paper are obtained with a special numerical toolkit made up of two codes. These are a laser-plasma relativistic interaction code called WAKE, recently modified in order to take gas ionization, plasma optical probing, and plasma temperature into account and a vacuum propagation code called IMAGE for ultrashort laser pulses.

First the code WAKE simulates the interaction of a very intense pump laser pulse with the gas medium and the action of the varying medium on a pair of probe laser pulses. The spatial regions covered by the simulation being typically of some Rayleigh lengths, the laser pulse distributions worked out by WAKE belong to an intermediate-field region. The actual frequency-domain interferometry being performed (as most optical diagnostics) in the near-field region, a second numerical code is needed for the propagation of the probe pulses through the optical collecting system and up to the spectrometer. The vacuum propagation code IMAGE has been conceived for broad spectrum waves such as ultrashort pulses.

We recall in the following the main features of the simulation code WAKE (more details on the structure of the algorithm can be found in recent specific papers[21,27]) and we describe the propagation code IMAGE. At the end of this section the wave propagation algorithms of the two codes are compared and discussed.

1. WAKE interaction code

WAKE is a 2-D particle code that can be used in cylindrical as well as in Cartesian geometry. Its algorithm is based upon three approximations: the ponderomotive and quasistatic approximations and an extended paraxial approximation.

Electron trajectories are governed by the ponderomotive force of the laser field and the self-consistent electric and magnetic fields of the plasma wake. Within this approximation, their low-frequency (i.e., plasma frequency band) components can be obtained by integration of the motion law

$$\frac{d}{dt}\,\overline{\mathbf{p}} = -e\left(\overline{\mathbf{E}} + \frac{\overline{\mathbf{v}}}{c} \wedge \overline{\mathbf{B}}\right) - \frac{e^2}{2\overline{\gamma} m_e c^2}\nabla\overline{|\widetilde{\mathbf{A}}_\perp|^2},$$

where the bar quantities are the low-frequency band components, $\mathbf{p}$ is the momentum, $\mathbf{v}$ is the velocity, $\mathbf{E}$ and $\mathbf{B}$ are, respectively, the electric and magnetic fields, and $\widetilde{\mathbf{A}}$ is the high-frequency band component of the vector potential. The quasistatic approximation consists of assuming that the form of the laser pulse, and consequently that of the wakefields, does not change significantly during the time it passes over individual electrons. Electron motion is then defined by this equation together with the definition of the high-frequency component of the momentum

$$\widetilde{\mathbf{p}} = \frac{e}{c}\,\widetilde{\mathbf{A}}$$

and of the average Lorentz factor

$$\overline{\gamma} = \sqrt{1 + \frac{|\overline{\mathbf{p}}|^2 + (e/c)^2 \overline{|\widetilde{\mathbf{A}}|^2}}{m^2 c^2}}.$$

Pulse propagation is solved in an extended paraxial approximation, realized by introducing the variable $\xi = ct - z$, and by separating the laser vector potential into a complex amplitude modulating a plane wave

$$\tilde{\mathbf{A}}(r,\xi,z) = \hat{\mathbf{A}}(r,\xi,z)\exp(ik_0\xi) + \text{c.c.},$$

where k_0 is the central wave number of the laser pulse. The evolution of the amplitude is obtained by dropping the highest-order term in the wave equation. This gives the equation

$$\left(\nabla_\perp^2 + 2ik_0\frac{\partial}{\partial z} - 2\frac{\partial^2}{\partial\xi\partial z}\right)\hat{\mathbf{A}} = -\frac{\omega_p^2}{\overline{\gamma}c^2}\hat{\mathbf{A}}, \tag{C1}$$

where ω_p is the classical plasma frequency. The ratio $\omega_p^2/\overline{\gamma}$ is obtained by averaging over an ensemble of particle trajectories.

Ionization of the gas medium is included in this version of the code. In the regime of pulse durations and intensities of interest, tunneling ionization[30,31] is dominant. Ionization rates are given by this model for any atomic ion. The formula for the tunneling ionization rate in terms of the amplitude E of the wave electric field is

$$R_t(\eta) = \omega_{\text{at}}C_{n*}^2\frac{(2l+1)(l+|m|)!}{2^{|m|}|m|!(l-|m|)!}\frac{\epsilon_i}{\epsilon_H}(2\eta)^{2n*-|m|-1} \times\exp(-\tfrac{2}{3}\eta),$$

where

$$\eta = \left(\frac{\epsilon_i}{\epsilon_H}\right)^{3/2}\frac{E_{\text{at}}}{E}$$

is the normalized electric field, ϵ_i is the ionization potential, l and m are the initial angular momentum quantum numbers of the ion, $n*$ is the effective final main quantum $n* = Z\sqrt{\epsilon_H/\epsilon_i}$, Z is the ionic charge after ionization, and $C_{n*}^2 = [2\exp(1)/n*]^{n*}/\sqrt{2\pi n*}$. The constants ω_{at} and E_{at} being, respectively, the typical atomic frequency and field, are $\omega_{\text{at}} = 4.16\times10^{16}\ \text{s}^{-1}$ and $E_{\text{at}} = 5.142\times10^9$ V/cm.

In the code, rates are used to compute the probabilities of ions to emit a number of electrons in an elementary time step. By recurrence one can show that the probability within an interval $\Delta\xi$ for a decay with n-electron emission is given by the formula

$$P_n(\Delta\xi) = (-1)^n\prod_{h=1}^{n}R_h\sum_{j=1}^{n}\frac{\exp(-R_j(\Delta\xi/c))}{\prod_{l=1,l\neq j}^{n+1}(R_j-R_l)},$$

where the kth ionization rate at the local value of the electric field has been indicated by R_k. Electrons are then emitted by a Monte Carlo procedure in agreement with these probabilities.

Because of the interaction with the electric field of the laser wave during the ionization process, electrons are given an initial transverse low-frequency drift according to a distribution. According to some theoretical results,[32] the average initial energy of the free electrons is very close to the ionization potential. In the code WAKE electrons are injected in the medium with a random initial energy belonging to a thermal equilibrium distribution at a given temperature. This temperature is arbitrarily set by an external parameter of the same order of the average ionization potential.

2. IMAGE propagation code

IMAGE is a spectral code for the propagation of electromagnetic waves in vacuum. With the spectral components of the waves being treated separately in the paraxial approximation, the narrow spectrum condition is not required. Three different transformations of the wave are taken into account by the code, namely the propagation from the interaction region up to a collecting lens, the modifications of phase and amplitude due to the interaction with a finite size collecting lens, and the final propagation from the lens to the output screen.

A well-known propagation integral for a monochromatic wave is the paraxial approximation of the Kirchhoff–Fresnel integral:[33]

$$\tilde{\mathbf{A}}(\mathbf{r},z,t) = \frac{k_0}{2\pi i}\frac{\exp(ik_0z)}{z}\exp\left(ik_0\frac{r^2}{2z}\right)\int\int\tilde{\mathbf{A}}(\mathbf{r}',0,t) \times\exp\left(ik_0\frac{r'^2}{2z} - ik_0\frac{xx'+yy'}{z}\right)dx'\,dy',$$

where the origin for the longitudinal distance z is taken at the input plane of the propagation. For a narrow spectrum wave, a phase and a slowly varying amplitude can be separated as in

$$\tilde{\mathbf{A}}(\mathbf{r},z,t) = \hat{\mathbf{A}}(\mathbf{r},\zeta,z)\exp(-ik_0\zeta) + \text{c.c.}, \tag{C2}$$

where we have introduced the spatial variable $\zeta = z - ct = -\xi$. One then obtains the transformation law for the slowly varying envelop

$$\hat{\mathbf{A}}(\mathbf{r},\zeta,z) = \frac{k_0}{2\pi i}\frac{\exp(ik_0(r^2/2z))}{z}\int\int\hat{\mathbf{A}}(\mathbf{r}',\zeta,0) \times\exp\left(ik_0\frac{r'^2}{2z} - ik_0\frac{xx'+yy'}{z}\right)dx'\,dy'. \tag{C3}$$

When the spectrum of the wave is not narrow, even if the definition of a main phase as in formula (C2) still applies, the slowly varying amplitude approximation is lost and the transformation law (C3) becomes incorrect. In this case the integral (C3) must be applied to every spectral component separately. After recombination of the spectral components, one obtains for the propagated wave

$$\hat{\mathbf{A}}(\mathbf{r},\zeta,z) = \frac{1}{(2\pi)^2}\frac{1}{iz}\int\exp(-i\kappa\zeta)(k_0+\kappa)\exp\left[i(k_0+\kappa)\frac{r^2}{2z}\right] \times\int\int\exp\left[-i(k_0+\kappa)\frac{xx'+yy'}{z} + i(k_0+\kappa)\frac{r'^2}{2z}\right] \times\int\exp(i\kappa\zeta')\hat{\mathbf{A}}(\mathbf{r}',\zeta',0)d\zeta\,dx'\,dy'\,d\kappa.$$

Since for the simulations shown in this paper we assumed rotational invariance around the optical axis for both the matter and the radiation distributions $\hat{\mathbf{z}}$, the above integral can be simplified. After integration over the rotation angle, the above transformation can be written as

$$\hat{\mathbf{A}}(r,\zeta,z)=\frac{1}{(2\pi)^2}\frac{1}{iz}F^{-1}\left\{(k_0+\kappa)\exp\left[i(k_0+\kappa)\frac{r^2}{2z}\right]\right.\times\int r'\exp\left[i(k_0+\kappa)\frac{r'^2}{2z}\right]J_0\left[i(k_0+\kappa)\frac{rr'}{z}\right]\left.\times F[\hat{\mathbf{A}}(r',\zeta,0)](\kappa)\right\}(\zeta), \tag{C4}$$

where J_0 is the Bessel function of first type and zero order and where the notation has been simplified by introducing the operators $F[f(\zeta)](\kappa)$ and $F^{-1}[g(\kappa)](\zeta)$, standing for the direct and inverse Fourier transforms of the functions $f(\zeta)$ and $g(\kappa)$, respectively.

With the suitable propagation distance z, this formula gives the vector potential distribution at the plane of the collecting lens. The effect of the lens on the wave is taken into account as a parabolic phase increment $kr^2/2f$, where f is the focal length,[34] and as a cut due to the physical size of the lens. Since this phase also depends on the exact wave number $\kappa=k_0+\kappa$, it must be added before the final inverse transform.

The last operation is the propagation from the lens to the output screen. The integral (C4) applies to this propagation as well.

Practically, IMAGE computes just one direct Fourier transform at the beginning of the calculation and works out the complete propagation of every spectral component up to the output screen. If the final time distribution of the wave is requested, IMAGE performs an inverse Fourier transform as the last calculation.

The relative phase of the two probe pulses is obtained as in the experiment by the Fourier transform of the spectral density, giving the autocorrelation function of the pair of pulses and the difference of their phases.

3. WAKE-IMAGE toolkit

Let us consider the wave equation (C1) and take the vacuum propagation limit

$$\left(\nabla_\perp^2+2ik_0\frac{\partial}{\partial z}-2\frac{\partial^2}{\partial\zeta\partial z}\right)\hat{\mathbf{A}}=0. \tag{C5}$$

This equation is solved by WAKE by direct numerical integration. In the case of narrow spectrum approximation the mixed derivative term can be dropped and the equation can be written as

$$\left(\nabla_\perp^2+2ik_0\frac{\partial}{\partial z}\right)\hat{\mathbf{A}}=0.$$

It is easy to show that the paraxial Kirchhoff–Fresnel integral (C3) is a solution of this paraxial monochromatic wave equation. So, since the Fourier transform of the equation (C5) gives

$$\left(\nabla_\perp^2+2i(k_0+\kappa)\frac{\partial}{\partial z}\right)F[\hat{\mathbf{A}}(r',\zeta,z)](\kappa)=0$$

one can state that each $k_0+\kappa$ spectral component of the integral (C4) is a solution of the corresponding spectral component of the paraxial wave equation. The integral (C4) is then a solution of the extended paraxial approximation of the wave equation in a vacuum.

This means that the two codes WAKE and IMAGE solve the same equation (C1). The approximation of the whole toolkit is then well defined and corresponds to a frequency-by-frequency paraxial approximation.

[1] J. Krall, G. Joyce, and E. Esarey, Phys. Rev. A **44**, 6854 (1991).
[2] See, e.g., *Advanced Accelerator Concepts*, edited by P. Schoessow, AIP Conference Proceedings No. 335 (AIP, New York, 1995).
[3] T. Tajima and J. M. Dawson, Phys. Rev. Lett. **43**, 267 (1979).
[4] N. E. Andreev, L. M. Gorbunov, V. I. Kirsanov, A. A. Pogosova, and R. R. Ramazahsvili, JETP Lett. **55**, 571 (1992); T. M. Antonsen, Jr. and P. Mora, Phys. Rev. Lett. **69**, 2204 (1992); P. Sprangle, E. Esarey, J. Krall, and G. Joyce, *ibid.* **69**, 2200 (1992).
[5] Y. Kitagawa, T. Matsumoto, T. Minamihata, K. Sawai, K. Matsuo, K. Mima, K. Nishihara, H. Azechi, K. A. Tanaka, H. Takabe, and S. Nakai, Phys. Rev. Lett. **68**, 48 (1992).
[6] C. E. Clayton, K. A. Marsh, A. Dyson, M. Everett, A. Lal, W. P. Leemans, R. Williams, and C. Joshi, Phys. Rev. Lett. **70**, 37 (1993).
[7] N. A. Ebrahim, J. Appl. Phys. **76**, 7645 (1994).
[8] F. Amiranoff, D. Bernard, B. Cros, F. Jacquet, G. Matthieussent, P. Mine, P. Mora, J. Morillo, F. Moulin, A. E. Specka, and C. Stenz, Phys. Rev. Lett. **74**, 5220 (1995).
[9] K. Nakajima, T. Kawakubo, H. Nakanishi, A. Ogata, Y. Kato, Y. Kitagawa, R. Kodama, K. Mima, H. Shiraga, K. Suzuki, T. Zhang, Y. Sakawa, T. Shoji, Y. Nishida, N. Yugami, M. Downer, D. Fisher, B. Newberger, and T. Tajima, Phys. Scr. **T52**, 61 (1994).
[10] A. Modena, Z. Najmudin, A. E. Dangor, C. E. Clayton, K. A. Marsh, C. Joshi, V. Malka, C. B. Darrow, C. Danson, D. Neeley, and F. N. Walsh, Nature (London) **377**, 606 (1995); C. Coverdale, C. B. Darrow, C. D. Decker, W. B. Mori, K. C. Tzeng, K. A. Marsh, C. E. Clayton, and C. Joshi, Phys. Rev. Lett. **74**, 4659 (1995); D. Umstadter, S.-Y. Chen, A. Maksimchuk, G. Mourou, and R. Wagner, Science **273**, 472 (1996); R. Wagner, S.-Y. Chen, A. Maksimchuk, and D. Umstadter, Phys. Rev. Lett. **78**, 3125 (1997).
[11] E. Esarey and P. Sprangle, IEEE Trans. Plasma Sci. **24**, 252 (1996).
[12] L. M. Gorbunov and V. I. Kirsanov, Sov. Phys. JETP **66**, 290 (1987).
[13] J. R. Marquès, J. P. Geindre, F. Amiranoff, P. Audebert, J. C. Gauthier, A. Antonetti, and G. Grillon, Phys. Rev. Lett. **76**, 3566 (1996).
[14] H. Hamster, A. Sullivan, S. Gordon, W. White, and R. W. Falcone, Phys. Rev. Lett. **71**, 2725 (1993).
[15] C. W. Siders, S. P. Blanc, D. Fisher, T. Tajima, M. C. Downer, A. Babine, A. Stepanov, and A. Sergeev, Phys. Rev. Lett. **76**, 3570 (1996).
[16] J. R. Marquès, F. Dorchies, P. Audebert, J. P. Geindre, F. Amiranoff, J. C. Gauthier, G. Hammoniaux, A. Antonetti, P. Chessa, P. Mora, and T. M. Antonsen, Jr., Phys. Rev. Lett. **78**, 3463 (1997).
[17] J. M. Dawson, Phys. Rev. **113**, 383 (1959).
[18] S. C. Wilks, J. M. Dawson, W. B. Mory, T. Katsouleas, and M. E. Jones, Phys. Rev. Lett. **62**, 2600 (1989); E. Esarey, A. Ting, and P. Sprangle, Phys. Rev. A **42**, 3526 (1990).
[19] S. Augst, D. Strickland, D. D. Meyerhofer, S. L. Chin, and J. H. Eberly, Phys. Rev. Lett. **63**, 2112 (1989); S. Augst, D. D. Meyerhofer, D. Strickland, and S. L. Chin, J. Opt. Soc. Am. B **8**, 858 (1991).
[20] J. P. Geindre, P. Audebert, A. Rousse, F. Fallies, J. C. Gauthier, A. Mysyrowicz, A. Dos Santos, G. Hammoniaux, and A. Antonetti, Opt. Lett. **19**, 1997 (1994).
[21] P. Mora and T. M. Antonsen, Jr., Phys. Rev. E **53**, R2068 (1996); Phys. Plasmas **4**, 217 (1997).
[22] W. Leemans, C. E. Clayton, W. B. Mori, K. A. Marsh, P. K. Kaw, A. Dyson, C. Joshi, and J. M. Wallace, Phys. Rev. A **46**, 1091 (1992); W. Leemans, C. E. Clayton, W. B. Mori, K. A. Marsh, A. Dyson, and C. Joshi, Phys. Rev. Lett. **68**, 321 (1992).
[23] B. M. Penetrante and J. N. Bardsley, Phys. Rev. A **43**, 3100 (1991).
[24] M. N. Rosenbluth and C. S. Liu, Phys. Rev. Lett. **29**, 701 (1972).

[25]A. Modena, Z. Najmudin, A. E. Dangor, C. E. Clayton, K. A. Marsh, C. Joshi, V. Malka, C. B. Darrow, and C. Danson, IEEE Trans. Plasma Sci. **24**, 289 (1996).
[26]A. R. Bell and P. Gibbon, Plasma Phys. Controlled Fusion **30**, 1319 (1988).
[27]L. Gorbunov, P. Mora, and T. M. Antonsen, Jr., Phys. Rev. Lett. **76**, 2495 (1996).
[28]G. Bonnaud, D. Teychenné, and J.-L. Bobin, Europhys. Lett. **26**, 91 (1994).
[29]E. Tokunaga, A. Terasaki, and T. Kobayashi, Opt. Lett. **17**, 1131 (1992).
[30]A. M. Perelomov, V. S. Popov, and M. V. Terent'ev, Sov. Phys. JETP **23**, 924 (1965).
[31]M. V. Ammosov, N. B. Delone, and V. P. Kraÿinov, Sov. Phys. JETP **64**, 1191 (1986).
[32]D. Bauer, Phys. Rev. A **55**, 2180 (1997).
[33]M. Born and E. Wolf, *Principles of Optics* (Pergamon, Oxford, 1987), p. 382.
[34]R. Guenther, *Optics* (Wiley, New York, 1990), p. 391.